2688800

Proceedings of the ASME 2014 33rd International Conference on Ocean, Offshore and Arctic Engineering
OMAE2014
June 8-13, 2014, San Francisco, California, USA

OMAE2014-24178

EXPERIMENTAL ANALYSIS OF A VERTICAL AND FLEXIBLE CYLINDER IN WATER: RESPONSE TO TOP MOTION EXCITATION AND PARAMETRIC RESONANCE

Guilherme R. Franzini♣,†,‡,*
Celso P. Pesce† PME [illegible]
Rafael Salles†
Rodolfo T. Gonçalves ‡
André L. C. Fujarra‡ PNV
Pedro Mendes♠

♣Computational Mechanics Laboratory (LMC) - Department of Structural Engineering and Geotechnics
†Offshore Mechanics Laboratory (LMO) - Department of Mechanical Engineering
‡Numerical Offshore Tank (TPN) - Department of Naval Architecture and Ocean Engineering
Escola Politécnica, University of São Paulo, Brazil

♠ Center of Research and Development, **Petrobras, Rio de Janeiro, Brazil**

ABSTRACT

Experiments with a flexible and submerged cylinder were carried out to investigate fundamental aspects of risers dynamics subjected to harmonic excitation at the top. The flexible model was designed aiming a high level of dynamic similarity with a real riser. Vertical motion, with amplitude of 1% of the unstretched length, was imposed with a device driven by a servomotor. Four values of the ratio between the exciting frequencies and the first eigenfrequency were investigated, namely $f_t : f_{N,1} = 1:3;\ 1:1;\ 2:1$ *and* $3:1$. *Cartesian coordinates of 43 monitored points positioned all along the span were experimentally acquired by using an optical tracking system. A simple Galerkin's scheme applied for modal decomposition, combined with standard Mathieu chart analysis, led to the idenfication of parametric resonances. A curious finding of this paper is that the Mathieu instability may simultaneously occur in more than one mode, leading to interesting dynamic behaviors, also revealed through standard power spectra analysis and displacement scalograms.*

Keywords: Experiments, flexible cylinder, imposed top motions.

INTRODUCTION

In the offshore scenario, structural elements such as risers and tethers are subjected to highly complex non-linear dynamic phenomena. Most of these behaviors are majorly regulated by tension, parameter that is responsible for what is commonly referred to as geometric rigidity stiffness; see, e.g., Pesce & Martins (2005) [1]. In the absence of current action, waves and, consequently, floating unity motions, riser tension is only function of space, governed by its own weight. On the other hand, motions of the floating unities, which are concomitantly caused by first and second orders free surface wave forces, by current and by wind, modulate riser tension in time, at large range of frequencies, from slow to high values.

Tension modulations are intrinsically associated to eigenfrequencies modulations, which may be a key point in the study of

---

[*] Address all correspondence to this author.

resonant fluid-structure interaction phenomena, such as vortex-induced vibrations (VIV); see, for example, Silveira *et al* (2007) [2], Joseffson & Dalton (2010) [3] and Srinil (2011) [4].

From the mathematical point of view, a riser subjected only to tension modulation can be modelled as a non-autonomous system, in which one parameter (geometric stiffness) is function of time. In this case, the Hill's equation governs the structural dynamics. Considering that the tension modulation is harmonic and monochromatic, a particular case of Hill's equation named Mathieu's equation is responsible for the dynamics. Deeper discussion regarding Hill's and Mathieu's equation can be found in several text books of dynamics, such as Meirovitch (2003) [5].

The most common form of Mathieu's equation is the non-damped one. However, physical systems are usually low-damped. Furthermore, under the fluid-structure interaction scope, hydrodynamic damping is usually modeled as a bi-linear function of velocity, as in Morrison's equation. Ramani *et al* (2004) [6] performed a deeper theoretical-numerical investigation of the Mathieu equation written as:

$$\ddot{u} + |\dot{u}|\dot{u} + (\bar{\delta} + \bar{\varepsilon}\cos t)u = 0 \qquad (1)$$

Consider firstly the non-damped case. The origin $x = 0$ is the trivial solution of the Mathieu's equation. However, depending on the combination of parameters $\bar{\delta}$ and $\bar{\varepsilon}$, this solution may be not stable. A common approach to check the instability of the origin is the so called Strutt diagram. The Strutt diagram allows to identify regions in the plane of parameters $\bar{\delta}$-$\bar{\varepsilon}$ where the trivial solution (the origin) is stable or unstable. These regions are defined by transition curves (following the nomenclature adopted in [6]) which can be numerically determined solving determinantal equations presented, for example, in [5].

Focusing now the damped case, [6] presents numerical simulations and analytical considerations regarding the behavior of Equation 1. Besides discussions on the structural bifurcation caused by the inclusion of the quadratic damping term, which transforms stable centers into stable focuses and unstable centers into unstable focuses separated by saddle points, by breaking homoclinic orbits, the authors discuss the existence of a secondary bifurcation, *"in which a pair of limit cycles come together and disapear (a saddle-node of limit cycles)"*, [6]. This secondary bifurcation emanates from the point $\bar{\delta} \approx 0.6304$ and $\bar{\varepsilon} \approx 1.4386$, following the local analytical approximation obtained in [6], $\bar{\delta} = -0.00534\bar{\varepsilon}^5 + 0.04716\bar{\varepsilon}^4 - 0.13696\bar{\varepsilon}^3 + 0.14908\bar{\varepsilon}^2 - 0.01551\bar{\varepsilon} + 0.58301$. Figure 1 illustrates the Strutt diagram obtained from Equation 1, together with a schematic view of the post-critical trajectories topology, corresponding to the various stable and unstable regions; [6].

Returning to the context of dynamics of risers and tethers, Mathieu instability and other phenomena have been focus of investigations during the last decades. Patel & Park (1991) [7] pointed out that, even in the instability region of the Strutt diagram, the oscillations are limited, due to the hydrodynamic damping term. In Simos & Pesce (1997) [8] is shown that the effects of tension variation along the length may play an important role in the dynamics of TLP tethers subjected do parametric excitation.

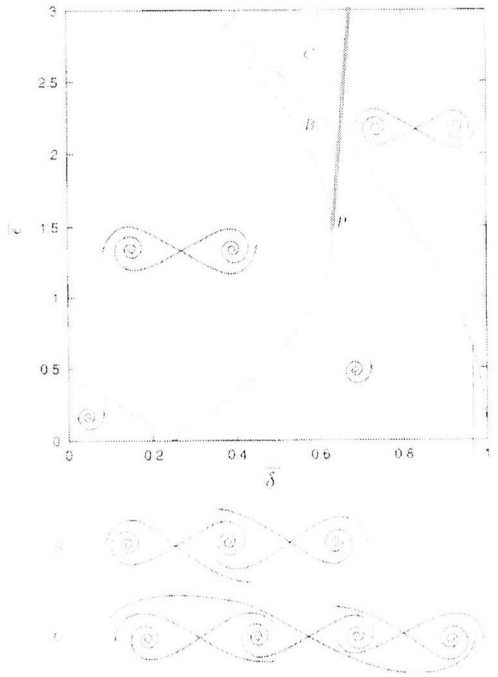

FIGURE 1. Strutt diagram obtained from Equation 1. Red line indicates the secondary bifurcation curve in the $\bar{\delta} - \bar{\varepsilon}$ plane. Focus on the first instability region. Adapted from [6].

Chatjigeorgiou & Mavrakos (2002) [9] considered the coupling of longitudinal and transversal displacements in the mathematical model. Among others features, the authors pointed out that the coupled system leads to modifications in the Strutt diagram. The parametric excitation of a nonlinear beam model which takes into account the effects of extensibility in the lateral motion was investigated numerically in Zeng *et al* (2008) [10], which highlights that the nonlinearities in the structural model are responsible for capturing the parametric excitation due to the surge motion of floating units. Yang *et al* (2013) [11] discussed the effects of irregular top excitation instead of a single harmonic. The numerical simulations presented in the latter paper showed significant differences between the Strutt diagram obtained for single-frequency or multi-frequency parametric excitation.

As can be seen in this brief introduction, a large number of theoretical and numerical investigations regarding the Mathieu instability in the context of risers and tethers is available. On the other hand, experimental data are rarer. The focus of this paper are to present experimental results of a flexible and immersed cylinder subjected to harmonic top motion excitation and to discuss the Mathieu instability by plotting onto the Strutt diagrams the experimental parameters obtained for the first three eigenmodes. For the sake of organization, this paper is composed by six sections. In the following one, the experimental arrangement and methodology are briefly described. In the second section, the model is experimentally characterized (in still water) in terms of eigenfrequencies and eigenmodes. The third section describes the modal analysis approach, followed by the presentation of an analytical model that will be employed aiming at plotting experimental data onto the Strutt diagram. The fifth section discusses the experimental results and the last one presents the final remarks and perspectives of future works.

EXPERIMENTAL ARRANGEMENT AND ANALYSIS METHODOLOGY

In laboratory tests, accounting for similarities with full scale is usually a hard task. The flexible cylinder employed in the investigation herein presented was designed aiming at reaching a high level of dynamic similarity with an 8" riser. The methodology used for the design of the scaled model is detailed in Rateiro *et al* (2012) [12]. Such a methodology is based on the Froude number similarity, related to the motions of the floating unity, caused by the incoming free surface waves.

A similitude investigation pointed out a family of dimensionless parameters that regulates the dynamics of a riser, as it might be regarded in [12]; all dimensionless numbers are presented in Table 1. Using Froude similarity in a usual riser of about 250 m in length and 219 mm in diameter with a reduced scale be taken of the order $\lambda = 100$, it was possible to build a model which fits the dimensions of the laboratory. Unfortunately scaling a 219 mm in diameter riser would result in a 2.19 mm in diameter model; such model, when the optical targets were pinned, would interfere with the shedding vortex phenomena. Furthermore structures with less than 10 mm in diameter are difficult to instrument, especially when optical sensors are intended to be used. Reynolds similarity is obviously not preserved, and, as pointed out in Rateiro *et al* [13], "*Adopting a distorted scale in diameter is usual in these circumstances, what helps increasing model Reynolds number. In fact, if* $\lambda_D < \lambda$ *is such a distorted scale, then* $Re_R = (\lambda\lambda_D)^{1/2}(Re_M)$. *This, however, might impair similarity regarding KC number, ...*". Anyhow, the experimental results at model scale may be used for comparing and validating numerical models. Despite the generality of the riser modelling methodology presented in [12] and [13], a single example of a 8 inches commercial pipe was chosen to be scaled. Corresponding parameters are shown in Table 2.

TABLE 1. Nondimensional parameters. Extracted from [12].

Number	Symbol	Representation
Froude number	$F_r = \frac{\omega A}{\sqrt{gL}}$	Dynamic motion in waves
Reynolds number	$Re = \frac{UD}{\nu}$	Inertial forces vs viscous forces
Strouhal number	$St = \frac{f_s D}{U}$	Vortex shedding frequency
Keulegan-Carpenter number	$KC = \frac{2\pi A}{D}$	Inertial forces vs drag forces
Structural damping	$\zeta = \frac{c}{c_c}$	Linear structural damping
Reduced velocity	$V_R = \frac{U}{f_n D}$	Normalized velocity in VIV
Reduced shedding frequency	$f_s^\star = \frac{f_s}{f_n} = = S_t \frac{U}{f_n D} = S_t V_r$	Vortex shedding normalized frequency
Reduced mass	$m^* = \frac{m}{m_D}$	Riser mass vs displaced mass
Added mass	$a = \frac{m_a}{m}$	Added mass vs riser mass
Bending stiffness	$K_f = \frac{\lambda_f}{L}$	Bending vs. geometrical stiffness
Axial stiffness	$K_a = \frac{EA}{T}$	Axial vs. geometrical stiffness

The model was made of a silicon tube with external diameter $D = 22.2$ mm, filled in with stainless steel micro-spheres. The size of the micro-spheres was adjusted in order to represent the scaled mass per unit length. The unstretched and stretched length were, respectively, $L_o = 2552$ mm and $L = 2602$ mm. The immersed length was $L_i = 2257$ mm. Both axial and bending stiffness (EA and EI) of the model were experimentally evaluated following a formulation based on large displacements, as can be found in Franzini *et al* (2012) [14]. Table 3 presents the model properties and Figures 2 and 3 show a picture of the experimental arrangement and a sketch of the experimental set-up respectively.

Harmonic displacements were imposed at the top by means of a in-house built servomotor device. The amplitude of the pre-

TABLE 2. Properties of the designed model and the as built one. Adapted from [12].

Data	Scale (1:100)	Designed model	As built
Internal diameter [mm]	1.826	15.800	15.800
External diameter [mm]	2.191	22.200	22.200
Immersed weight [N/m]	0.726	7.308	7.88
Axial rigidity stiffness EA [kN]	2.362	1.910	1.2
Bending stiffness EI [Nm^2]	1.20E-03	8.86E-03	5.60E-02
Added mass $a = m_a/m$	0.522	0.520	0.48

TABLE 3. Complementary model properties.

Property	Value
Unstretched length L_o	2552 mm
Stretched length L	2602 mm
Immersed length L_i	2257 mm
Mass ratio parameter m^*	3.48
Aspect ratio L_i/D	102
L/D	117
Static tension at the top T_t	40 N

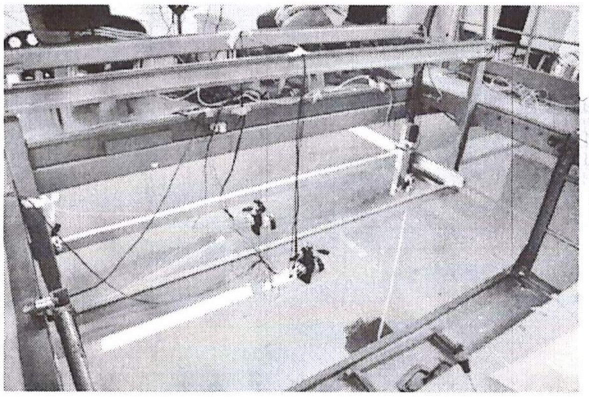

(a) General view of the experimental set-up.

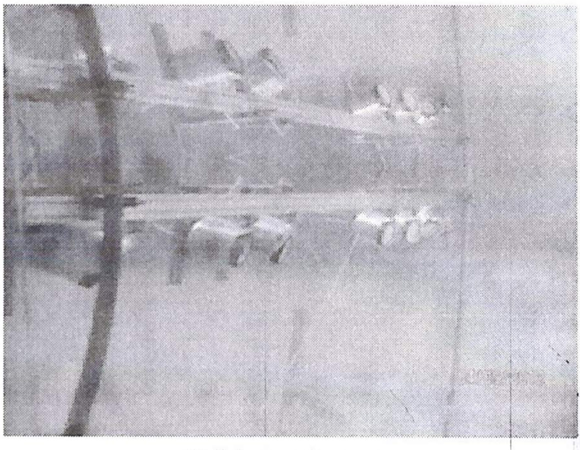

(b) Submerged cameras.

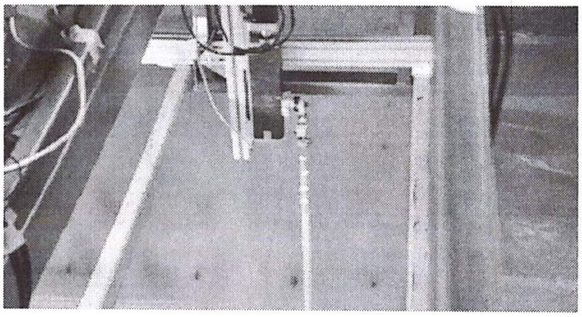

(c) Servomotor device.

FIGURE 2. Pictures of the experimental arrangement.

scribed top motion was $A_t/L_o = 1\%$, a small value indeed, but representative of usual riser dynamics. Six values of top motion frequency were investigated, namely, $f_t : f_{N,1} = 1:3$; $1:2$; $2:3$; $1:1$; $2:1$ and $3:1$, where $f_{N,1}$ is the first eigenfrequency evaluated from free decay tests carried out in still water. Due to limitations in the length of the paper, the cases $1:2$ and $2:3$ will not be discussed herein. The cartesian coordinates of 43 reflexives and almost non-intrusive targets placed along the model were measured through a Qualisys® optical tracking system. Six submerged cameras acquired the data from 38 underwater targets and two aerial cameras acquired the data from the remaining targets. The calibration quality of the optical motion capture system and its uncertainties depend on the number of cameras, the quality of the targets reflection, calibration time and distance to targets. At the end of the calibration process, the optical motion

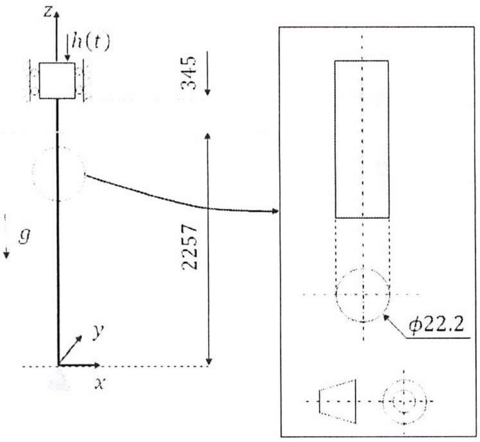

FIGURE 3. Sketch of the experimental set-up.

capture system provided the standard deviation from the known measures. This value represents the measurement uncertainty. In that calibration process, such a value was around 0.1 mm, so of order $D/200$. The uncertainty of the measurement is larger than the uncertainty of the displacement imposed by the servomotor device.

The model was mounted at the towing carriage of IPT (the São Paulo State Technological Research Institute). The lower end of the model was clamped to a support, rigidly fixed to the bottom of the carriage, while the upper end was clamped to a load cell, which measured the vertical component of tension. Typical vertical misalignment is close to 1% of the stretched length. All the data were acquired with sample frequency $f_{sp} = 60$ Hz, runs lasting 120 s.

Herein, z represents the spanwise position, measured from the lower end of the cylinder. All the displacements are normalized with the diameter, i.e., $x^*(t) = x(t)/D$, $y^*(t) = y(t)/D$ and $z^*(t) = z(t)/D$.

Regarding analysis methodology, we focus on the presentation of amplitude scalograms $x^*(z^*,t)$, power density spectra (PSD) $S_x(z^*,f)$ and the Strutt diagrams. It is worth mentioning that, as this paper focus on the case without carriage speed, the response in the x direction is expected to be similar to that obtained in the y direction, except for unavoidable asymmetries in the experimental set-up. Experiments with concomitant parametric excitation and towing speed were also carried out and will be discussed in future works.

CHARACTERIZATION

Firstly, free decay tests driven by impacts at the midspan were carried out in still water. The spanwise distribution of the PSD is shown in Figure 4, from which the following relation could be extracted for the the n-eigenfrequency:

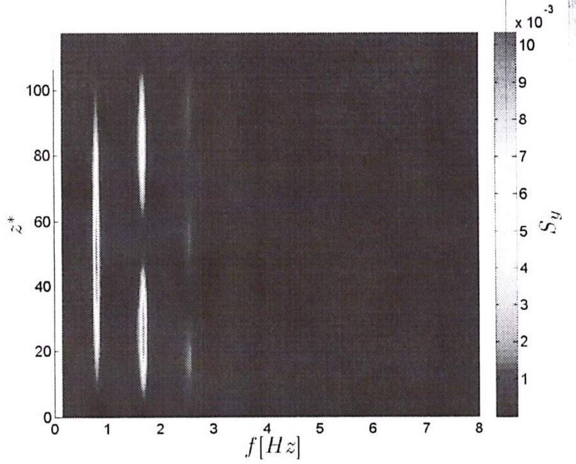

FIGURE 4. Spanwise distribution of PSD. Free decay tests in still water.

$$f_{N,n} = n0.84\text{Hz}, \quad n = 1,2,3 \tag{2}$$

Given that the bending stiffness is very small and the vertical flexible cylinder is long ($L/D > 100$), Bessel's functions, or even WKB approximate solutions, would be a proper choice for the eigenmodes (see, for example, Pesce *et al* (1999) [15] and Chatjigeorgiou (2008) [16]). However, for the sake of simplicity, the eigenmodes $\psi_n(z)$ are here simply represented by sinusoidal functions, as Equation 3:

$$\psi_n(z) = \sin\left(n\pi\frac{z}{L}\right) \quad n = 1,2,3 \tag{3}$$

In fact and strictly speaking, sinusoidal function represent the eigenmodes of a horizontal tensioned string. The following section focus on the presentation of the modal analysis approach employed in the analytical model that supports the discussion of the experimental results.

MODAL ANALYSIS

As discussed in the previous section, sinusoidal functions consist on a first and simple choice to represent the eigenmodes $\psi_n(z)$. In the present section, the focus is the procedure to obtain the time series $u_n^*(t) = u_n(t)/D$ that represents the oscillating amplitude of the nth-eigenmode. For this, consider that, at a given instant t, $x(z,t)$ represents the oscillatory part of the *elastica* of the model. The amplitude of the n-eigenmode can be obtained by standard orthogonal projection, written as:

$$u_n(t) = \frac{< x(z,t), \psi_n(z) >}{< \psi_n(z), \psi_n(z) >} = \frac{\int_0^L x(z,t)\psi_n(z,t)dz}{\int_0^L \psi_n^2(z,t)dz} \tag{4}$$

Notice that Equation 4 allows to investigate the dynamics of the system by just considering a few eigenmodes, instead of the 43 time series of cartesian coordinates. Table 4 presents the characteristic amplitude (obtained by computing the average of the 10% of the highest peaks, as in Franzini *et al* (2013) [17]) and the dominant frequency f_d of the modal amplitude time series.

TABLE 4. Characteristic amplitude and frequency of the modal amplitude time series.

$f_t : f_{N,1}$	u_n^0/D			$f_d/f_{N,1}$		
	$n=1$	$n=2$	$n=3$	$n=1$	$n=2$	$n=3$
$1:3$	0.10	0.05	0.04	1.00	0.33	0.33
$1:1$	0.38	0.18	0.10	1.00	1.00	2.00
$2:1$	0.63	0.45	0.16	1.00	2.00	2.00
$3:1$	0.05	0.12	0.45	3.00	3.00	3.00

The appendix presents the modal amplitude time series $u_n(t)/D$ obtained, together with the corresponding PSD, as well as phase portraits $\dot{u}_n(t)/(\omega_d D)$ *vs* $u_n(t)/D$. An interesting aspect that can be seen in Figure 10(b) (see appendix) indicates that the flexible cylinder may oscillate with the shape of the second eigenmode and the frequency of the first eigenmode. This is, in fact, a result of modelling an intrinsic nonlinear structure and related phenomena by employing linear modes. Ongoing researches on this subject make use of nonlinear modes, which carry richer information on oscillation frequencies, amplitudes and velocities, as an alternative analytical approach for this problem. The reader interested in theoretical discussion and applications of nonlinear modes is referred to Shawn & Pierre (1991,1994) [18], [19].

ANALYTICAL MODEL

In this analytical model, the bending stiffness is neglected when compared to the geometric stiffness. In fact, bending stiffness effect is relatively small, and, in the case of low numbered modes, confined only to the cylinder extremities; see [1] and [20]. However, this effect could be considered, from a WKB approximation, as shown in [15] and Chatjigeorgiou (2008b) [16], or, alternatively, by tranforming the fourth-order differential equation into a second-order one, substituting the bending stiffness term with an additional and approximatly equivalent geometric stiffness one; see Mazzilli *et al* (2014) [21]. Following the simplest approach, the lateral displacement is given by the equation of a vertical string subjected to a nonlinear damping term, in the form of Equation 6.

$$\begin{aligned} m_t \frac{\partial^2 x(z,t)}{\partial t^2} + \frac{1}{2}\rho D C_D \frac{\partial x(z,t)}{\partial t}\left|\frac{\partial x(z,t)}{\partial t}\right| \\ -\frac{\partial}{\partial z}\left(T(z,t)\frac{\partial x(z,t)}{\partial z}\right) = 0 \end{aligned} \tag{5}$$

In the previous equation, $m_t = m_l + m_{ad}$ is the total mass per unit length (added mass m_{ad} included), C_D is the drag coefficient (supposed independent of the spanwise position) and ρ is the fluid density. The total tension is $T(z,t) = T_t - \gamma(L-z) + T_d$, where γ is the immersed weight and $T_d = \frac{EA}{L_0} A_t \cos(\omega_t t)$ is the dynamic tension induced by the top motion. Albeit it is well know that added mass and drag coefficients depend on the oscillation amplitude, in this paper these parameters will be considered constant and equal to 1 and 1.2 respectively.

Considering $x(z,t) = \psi_n(z)u_n(t)$ and applying the Galerkin approach (multiplying Equation 6 by $\psi_n(z) = \sin\left(n\pi\frac{z}{L}\right)$ and integrating along the cylinders's length), the following Equation is obtained:

$$M_n\ddot{u}_n + \beta_n|\dot{u}_n|\dot{u}_n + (\eta_n + \xi_n\cos(\omega_t t))u_n = 0 \tag{6}$$

Where:

$$M_n = \int_0^L m_t \psi_n^2(z)dz = (m_l + m_{ad})\frac{L}{2} \tag{7}$$

$$\beta_n = \int_0^L \frac{1}{2}\rho C_D D|\psi_n(z)|\psi_n^2(z)dz \tag{8}$$

$$\eta_n = \left(\frac{n\pi}{2}\right)^2\left(2\frac{T_t}{L} - \gamma\right) \tag{9}$$

$$\xi_n = \left(\frac{n\pi}{2}\right)^2\left(\frac{EA}{L_o}\right)\frac{2A_t}{L} \tag{10}$$

Notice that $\omega_{N,1} = \sqrt{\eta_1/M_n}$ is the theoretical value of the first eigenfrequency (in rad/s). Computing η_1 and M_n, we obtain $\omega_{N,1} = 5.24$ rad/s, which is, practically, the experimental result for the first eigenfrequency (i.e., $2\pi \times 0.84 = 5.28$ rad/s), as already presented.

Aiming at obtaining a classical form of Mathieu's equation, Equation 6 can be written considering the non-dimensional time $2\tau = \omega_t t$, leading to Equation 11.

$$\frac{d^2u_n(\tau)}{d\tau^2} + 2\mu_n \frac{du_n(\tau)}{d\tau}\left|\frac{du_n(\tau)}{d\tau}\right| + (\delta_n + 2\varepsilon_n cos(2\tau))u_n(\tau) = 0 \tag{11}$$

Where:

$$\mu_n = \frac{\beta_n}{2M_n} \tag{12}$$

$$\delta_n = \frac{4\eta_n}{M_n\omega_t^2} \tag{13}$$

$$\varepsilon_n = \frac{2\xi_n}{M_n\omega_t^2} \tag{14}$$

It is important to highlight the differences between the alterative forms of Mathieu's equation, Equations 1 and 11. The differences, in form and consequently in the definition of the parameters, are related to the scaling of both, the nondimensional time and the parametric excitation amplitude.

The experimental data for δ_n and ε_n are presented in Table 5. These values will be plotted in the Strutt diagram for the first three eigenmodes.

TABLE 5. Experimental points in the δ_n-ε_n plane. Bolded points are close to the transition curves or inside unstable regions.

$f_t : f_{N,1}$	δ_n			ε_n		
	$n=1$	$n=2$	$n=3$	$n=1$	$n=2$	$n=3$
1 : 3	35.54	142.17	319.88	7.02	28.09	63.19
1 : 1	**3.95**	15.80	35.54	**0.78**	3.12	7.02
2 : 1	**0.99**	**3.95**	8.89	**0.20**	**0.78**	1.76
3 : 1	0.44	1.76	**3.95**	0.09	0.35	**0.78**

The following section discusses the experimental results. This discussion is carried out focusing on the time series $x^*(z^*,t)$ plotted in scalograms, the spanwise distribution of corresponding PSD $S_x(z^*,f)$, and on results of modal decomposition analysis plotted onto Strutt diagrams. Such results are complemented in the appendix, with time series of modal amplitude and corresponding power spectra, as well as modal phase portraits.

RESULTS AND DISCUSSION

Figure 5 presents the scalograms of the oscillatory component of $x^*(z^*,t)$ for a time interval of 10s. Aiming at a better visualization, the colorbars do not follow the same scale. Figure 6 presents the spanwise spectral distribution $S_x(z^*,f)$ computed from the whole acquisition time (120s).

Considering the 1 : 3 case, Figure 5(a) indicates a standing wave pattern response. It can be noticed that the oscillations near the bottom are larger than those close to the top, as expected, since tension decreases with depth. This result is also observed in the $S_x(z^*,f)$ plot shown in Figure 6(a), where sub-harmonic responses clearly show up. The same plot also reveals other spectral components ar $f : f_{N,1} = 1 \pm 1/3$.

The multi-component character of the response is also observed in the $f_t : f_{N,1} = 1 : 1$ case, presented in Figures 5(b) and 6(b). The $S_x(z^*,f)$ spectrum is mainly composed by two harmonics, at $f_{N,1}$ and $2f_{N,1}$. The scalogram indicates a marked presence of travelling waves, contrary to the $f_t : f_{N,1} = 1 : 3$ case. Furthermore, the celerity of the travelling waves, given by the inclination of each trace of the scalogram depends on the position z^*. This fact is not surprising, since the tension decreases with depth.

The scalogram corresponding to the $f_t : f_{N,1} = 2 : 1$ case is qualitatively distinct from the previous ones. It reveals an interesting dynamic pattern, where dominant responses at two modes clearly coexist, the first and the second one, besides a smaller contribution of the third mode. A pitch-fork like figure may be seen forming at midspan, alternately reinforcing vibrations of both dominant modes, along the upper (sharper) or the lower (fuzzier) part of the cylinder. A clearer picture of such an interesting dynamic behavior may be formed by analysing the corresponding modal phase portraits presented in the appendix. Still considering the $f_t : f_{N,1} = 2 : 1$ case, the spectrum $S_x(z^*,f)$ also reveals the components $f = f_{N,1}$ and $f = 2f_{N,1}$, but the higher amount of energy is not related to the frequency of the top motion.

Finally, the case $f_t : f_{N,1} = 3 : 1$ is also distinct from the others analysed in this section. The $S_x(z^*,f)$ plot (see Figure 6(d)) is monochromatic and narrowbanded centered at $f = 3f_{N,1} = f_t$, and the scalogram presented in Figure 5(d) clearly reveals a stable and repetitive standing wave pattern in the third eigenmode. Hence, for this condition of prescribed top motion, the response in mainly due to the external excitation.

Now, we change the focus to the analysis of the Mathieu instability by using the Strutt diagrams for the first, second and third eigenmodes. The results of the Strutt diagram will be correlated with the scalograms and spectra presented in Figures 5 and 6.

The Strutt diagrams for the first three eigenmodes are presented in Figure 7. Firstly, let us consider only the first eigenmode (see Figure 7(a)). From the mentioned figure, it is clearly visible that the green square is in a unstable region of the Strutt diagram. Hence, the top excitation frequency $f_t : f_{N,1} = 2:1$ leads to Mathieu instability for the first eigenmode. It is worth to emphasize that, despite the combination of the values of the parameters δ and ε leading to the unstable region, the amplitude of motion is relatively small. This fact is associated with the nonlinear damping term in Equation 11 and was already pointed out by [7]. Still considering the first eigenmode, the red square, which corresponds to the $f_t : f_{N,1} = 1:1$ case, is at a transitional curve. Thus, in this case we can also expect oscillations with non negligible amplitudes. Notice also that, as the amplitude of the parametric excitation is small, neither the $f_t : f_{N,1} = 2:1$ case or the $f_t : f_{N,1} = 1:1$ one are close to the secondary bifurcation curve. Such a curve is graphed in red and was constructed from [6], after re-scaling from $\bar{\delta} - \bar{\varepsilon}$ to the $\delta - \varepsilon$ diagram.

The Strutt diagram for the second eigenmode is shown in Figure 7(b). Notice that, the $f_t : f_{N,1} = 2:1$ ($f_t : f_{N,2} = 1:1$) case is practically at a transition curve, such that Mathieu's instability may be clearly explained. On the other hand, the points corresponding to the cases $f_t : f_{N,1} = 1:1$ and $f_t : f_{N,1} = 3:1$ are close enough to the transition to instability, such that any small perturbation in one of the parameters, as for instance in the added mass coefficient, may trigger Mathieu instability for the second eigenmode, in this excitation frequency as well. This discussion agrees with the characteristic amplitude u_2^0 presented in Table 4, for which the higher value is related to $f_t : f_{N,1} = 2:1$, but with non-negligible oscillations in the cases $f_t : f_{N,1} = 1:1$ and $f_t : f_{N,1} = 3:1$.

The Strutt diagram for the third eigenmode is presented in Figure 7(c). The latter plot indicates that the top excitation with frequency $f_t : f_{N,1} = 3:1$ leads to Mathieu instability. In the same plot, the green square is located close to a transition curve. Once again, the results from Table 4 agree with those predicted by the Strutt diagram, with the higher amplitude u_3^0/D being observed for the $f_t : f_{N,1} = 3:1$ case. Furthermore, the dominance of vibration of the third eigenmode in the condition with top motion excitaion with $f_t : f_{N,1} = 3:1$ has already been discussed in the analysis of the scalograms and the PSD plots (see Figures 5(d) and 6(d) respectively).

Up to this point, we discussed the Strutt diagram based on the modal amplitude time series for each of the chosen eigenmodes $\psi_n(z)$, $n = 1,2,3$. Now, we turn our attention to investigate Mathieu instabilities for each excitation frequency. This approach allows a straightforward way to interpret the scalograms and the PSD plots presented in Figures 5 and 6.

The first case analysed is that in which $f_t : f_{N,1} = 1:1$, marked as red squares in Figure 7. For this excitation condition, only the first eigenmode is at a transition curve, hence subjected to significant oscillations. This fact is confirmed by modal amplitudes distribution presented in Table 4.

Considering now the case with excitation frequency $f_t : f_{N,1} = 2:1$, the green squares in Figure 7 indicate not only the Mathieu instability in the first eigenmode (Figure 7(a)), but also

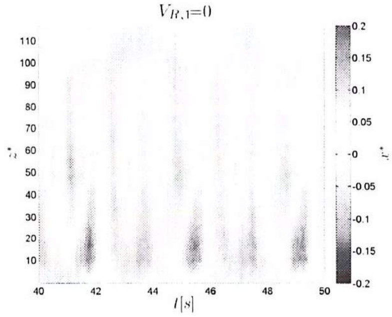

(a) $f_t : f_{N,1} = 1:3$.

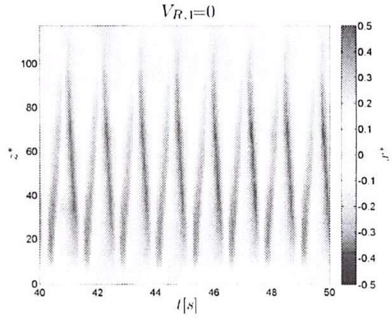

(b) $f_t : f_{N,1} = 1:1$.

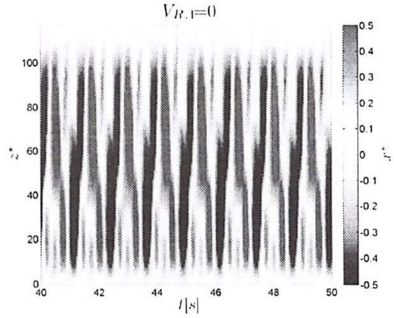

(c) $f_t : f_{N,1} = 2:1$.

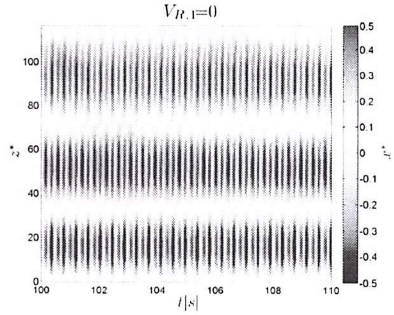

(d) $f_t : f_{N,1} = 3:1$.

FIGURE 5. Scalograms $x^*(z^*, t)$. Only 10s of acquisition are show

the possibility of this instability in the second and third eigenmodes (Figures 7(a) and 7(c) respectively). These results may justify the modal amplitude distribution presented in Table 4. Moreover, the composition of three modes may be related to the alternating "fork" pattern verified in the scalogram shown in Figure 5(c).

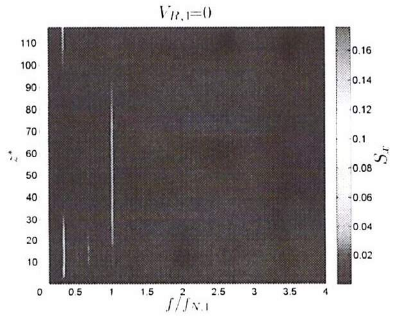

(a) $f_t : f_{N,1} = 1:3$.

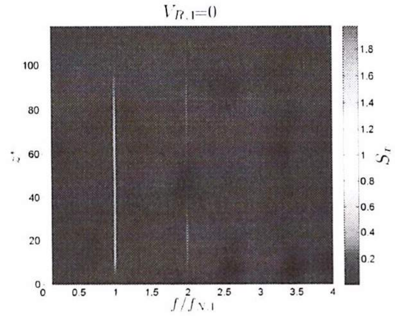

(b) $f_t : f_{N,1} = 1:1$.

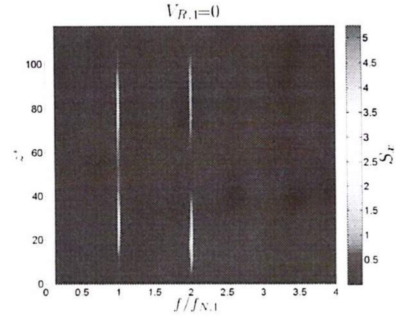

(c) $f_t : f_{N,1} = 2:1$.

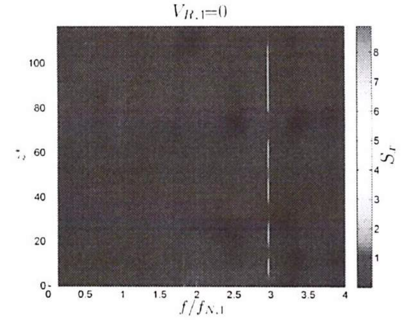

(d) $f_t : f_{N,1} = 3:1$.

FIGURE 6. PSD spectra $S_x(z^*, f)$.

Finally, in the case with $f_t : f_{N,1} = 3:1$, the blue square in Figure 7(c) reveals that the third eigenmode is at a transition curve, whereas for the others cases, the referred marker is inside stable regions. This result totally agree with the character of both the corresponding scalogram and spanwise PSD plot shown, respectively, in Figures 5(d) and 6(d), as well as with the characteristic oscillation amplitude u_3^0 results presented in Table 4.

Before the presentation of the final remarks, a last aspect should be highlighted. The use of sinusoidal functions as a decomposition set showed, so far, to be a good choice, balancing simplicity and quality of results. Further investigations may take into account other set of functions in the Galerkin's decomposition scheme, by using more sophisticated approximations to the eigenmodes, as Bessel's or WKB asymptotics. However, other issues, as orthogonality properties should be properly worked out.

FINAL REMARKS

An experimental investigation with a flexible and immersed vertical cylinder subjected to harmonic and vertical top motions was carried out and the results for four excitations frequencies were analysed and discussed. The flexible cylinder was designed aiming a certain degree of similarity with a 8'' riser. Cartesian coordinates of 43 targets placed along the model were acquired by using an optical system. The top motion was imposed by means of a in-house built servodriver device.

The excited lateral displacement was analysed by means of displacement scalograms and spanwise distribution of the Power Spectrum Density (PSD). In the case in which the top motion frequency obeys the relation $f_t : f_{N,1} = 1:1$, the scalogram indicated the presence of a travelling-wave pattern and the PSD plot $S_x(z^*, f)$ highlighted the predominance of the first two eigenmodes in the response. In the $f_t : f_{N,1} = 2:1$ case, the $S_x(z^*, f)$ also indicated the predominance of the first and second eigenmodes, but the scalogram revealed an alternating "fork pattern". The higher top motion frequency tested corresponds to $f_t : f_{N,1} = 3:1$. Contrary to the previous ones, the latter condition was characterized by the predominance of a standing-wave pattern with the shape of the third eigenmode.

Aiming at a deeper investigation into the parametric excitation that characterizes the dynamics of the flexible cylinder subjected to top motion, a modal decomposition approach was employed jointly with Strutt diagrams. The Mathieu instability was studied both in terms of eigenmodes and in terms of excitation frequencies.

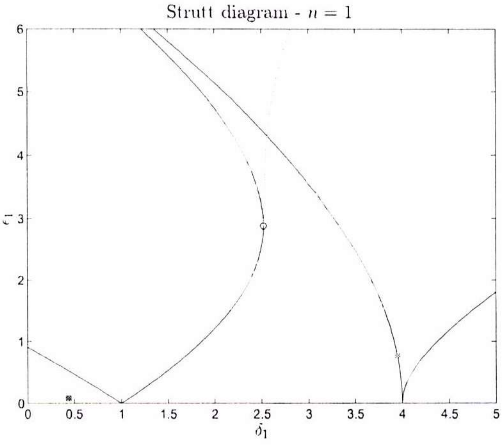

Strutt diagram - $n = 1$

(a) First eigenmode.

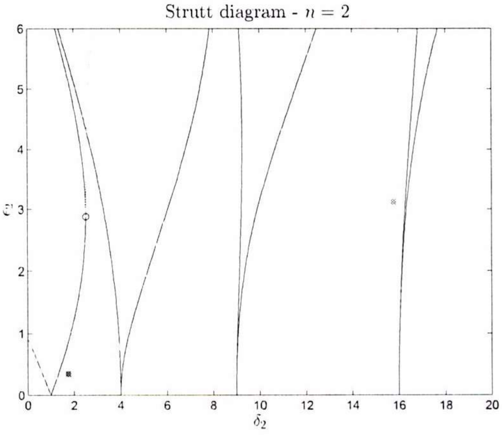

Strutt diagram - $n = 2$

(b) Second eigenmode.

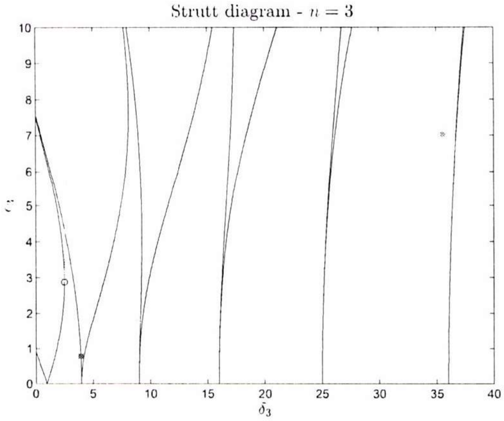

Strutt diagram - $n = 3$

(c) Third eigenmode.

FIGURE 7. Strutt diagrams. Red: $f_t : f_{N,1} = 1 : 1$; Green: $f_t : f_{N,1} = 2 : 1$; Blue: $f_t : f_{N,1} = 3 : 1$. Results for the condition $f_t : f_{N,1} = 1 : 3$ are within the stable region and are not shown.

In the case in which $f_t : f_{N,1} = 1 : 1$, the Strutt diagram pointed out the Mathieu instability in the first eigenmode. On the other hand, for the case $f_t : f_{N,1} = 2 : 1$, the analysis of the Strutt diagram allowed to assert that the Mathieu instability is possible to occur in more than one eigenmode. This fact was verified checking the modal amplitude time series.

One of the main contributions of this paper is an approach (based on modal analysis) for correlation of experimental results of a vertical cylinder subjected to parametric excitation with a classical and theoretical procedure for checking the Mathieu instability. It was found that, depending of the combinations of modal parameters δ_n and ε_n, parametric instabilities may occur in more than one eigenmode simultaneously. This fact may be important in the dynamics of top tension risers (TTR) or TLP tethers.

It has also been found that the amplitude of parametric excitation used in the experiments was not large enough to even approach the curve of secondary instability related to quadratic damping, which emerges from the first Mathieu instability tongue, as studied in [6].

Finally, further work on vertical cylinder dynamics will include the analysis of experimental results of concomitant Vortex-Induced Vibration (VIV) and parametrically excited vibrations, already obtained during the same research project. Besides, further investigation and discussions are planned, on alternative modal representations, as well as on reduced order modelling techniques, based not only on Mathieu's, but also on coupled Mathieu-Duffing's and van der Pol oscillators.

ACKNOWLEDGMENT

This work has been carried out after a research project sponsored by Petrobras. The first author acknowledges FAPESP for his post-doctoral scholarship, process no. 2013/09802-2. The second and third authors acknowledge CNPq, for the research grant 30.3838/2008-6 and the graduate scholarship 131549/2013-8. Special thanks to the IPT technical staff for helping with the experiments.

REFERENCES

[1] Pesce, C. P., and Martins, C. A., 2005. *Numerical computation of riser dynamics, Ch. 7 in Numerical modeling in Fluid-Structure Interaction*. Editor Subrata Chakrabarti, WIT Press, p. 253-309.

[2] Silveira, L. M. Y., Martins, C. A., Cunha, L. D., and Pesce, C. P., 2007. "An investigation on the effect of tension variation on VIV of risers". In Proceedings of the 26th International Conference on Offshore Mechanics and Arctic Engineering - OMAE 2007.

[3] Joseffson, P. M., and Dalton, C., 2010. "An analytical/computational approach in assessing vortex-induced vi-

bration of a variable tension riser". *Journal of Offshore Mechanics and Arctic Engineering,* ***132***.

[4] Srinil, N., 2011. "Analysis and prediction of vortex-induced vibrations of a variable-tension vertical risers in linearly sheared currents". *Applied Ocean Research,* ***33***, pp. 41–53.

[5] Meirovitch, L., 2003. *Methods of Analytical Dynamics*. Dover Publications.

[6] Ramani, D. V., Keith, W. L., and Rand, R. H., 2004. "Perturbation solution for secondary bifurcation in the quadratically-damped Mathieu equation". *International Journal of Non-Linear Mechanics,* ***39***, pp. 491–502.

[7] Patel, M. H., and Park, H. I., 1991. "Dynamics of tension leg platform tethers at low tension. Part I - Mathieu stability at large parameters". *Marine Structures,* ***4***, pp. 257–273.

[8] Simos, A. N., and Pesce, C. P., 1997. "Mathieu stability in the dynamics of TLP's tethers considering variable tension along the length". In Transactions on the Built Enviroment, vol. 29. Originally presented at Offshore Brazil 1997.

[9] Chatjigeorgiou, I. K., and Mavrakos, S. A., 2002. "Bounded and unbounded coupled transverse response of paraparametric excited vertical marine risers and tensioned cable legs for marine applications". *Applied Ocean Research,* ***24***, pp. 341–354.

[10] Zeng, X., Xu, W., Li, X., and Wu, Y., 2008. "Nonlinear dynamic responses of the tensioned tether under parametric excitation". In Proceedings of the Eighteenth (2008) International Offshore and Polar Engineering Conference - ISOPE 2008.

[11] Yang, H., Xiao, F., and Xu, P., 2013. "Parametric instability prediction in a top-tensioned riser in irregular waves". *Ocean Engineering,* ***70***, pp. 39–50.

[12] Rateiro, F., Pesce, C. P., Gonçalves, R. T., Franzini, G. R., Fujarra, A. L. C., Salles, R., and Mendes, P., 2012. "Risers model tests: Scaling methodology and dynamic similarity". In Proceedings of the The 22nd International Ocean and Polar Engineering Conference, ISOPE 2012.

[13] Rateiro, F., Gonçalves, R. T., Pesce, C. P., Fujarra, A. L. C., Franzini, G. R., and Mendes, P., 2013. "A model scale experimental investigation on vortex-self induced vibrations (VSIV) of catenary risers". In Proceedings of the ASME2013 32th International Conference on Ocean, Offshore and Arctic Engineering-OMAE2013.

[14] Franzini, G. R., Rateiro, F., Gonçalves, R. T., Pesce, C. P., and Mazzilli, C. E. N., 2012. "An experimental assessment of rigidity parameters of a small-scaled riser model". In Proceedings of the Pan American Congress of Applied Mechanics (PACAM XII).

[15] Pesce, C. P., Fujarra, A. L. C., Simos, A. N., and Tannuri, E. A., 1999. "Analytical and closed form solutions for deep water riser-like eigenvalue problem". In Proceedings of the Ninth (9th) International Offshore and Polar Engineering Conference.

[16] Chatjigeorgiou, I. K., 2008. "Application of the WKB method to catenary-shaped slender structures". *Mathematical and Computer Modelling,* ***48***, pp. 249–257.

[17] Franzini, G. R., Gonçalves, R. T., Meneghini, J. R., and Fujarra, A. L. C., 2013. "One and two degrees-of-degrees vortex-induced vibration experiments with yawed cylinders". *Journal of Fluids and Structures*.

[18] Shaw, S. W., and Pierre, C., 1991. "Non-linear normal modes and invariant manifolds". *Journal of Sound and Vibration,* ***150***, pp. 170–173.

[19] Shaw, S. W., and Pierre, C., 1993. "Normal modes for nonlinear vibratory systems". *Journal of Sound and Vibration,* ***164***, pp. 85–124.

[20] Chatjigeorgiou, I. K., 2008. "Solution of the boundary layer problem for calculating the natural modes of riser-type slender structures". *Journal of Offshore Mechanics and Arctic Engineering,* ***130***, pp. 011003–011003–7.

[21] Mazzilli, C. E. N., Lenci, S., and Demeio, L., 2014. "Nonlinear free vibrations of tensioned vertical risers". In Proceedings of 8th european nonlinear dynamics conference - ENOC2014 (to appear).

APPENDIX: MODAL AMPLITUDE TIME SERIES AND PHASE PORTRAITS

This appendix presents the modal amplitude time series, the corresponding spectra and modal phase portraits. It is readly seen from the time series, spectra and modal phase portraits, that the modal dynamics is, as expected, periodic or *quasi*-periodic. A closer analysis of the graphs shown below give complementary contributions to what have been discussed in the main sections, as for example, the clear coexistence of two dominant modes vibrating as response to the 2 : 1 excitation. Poincaré's sections could also be constructed to study the cases of *quasi*-periodicity further.

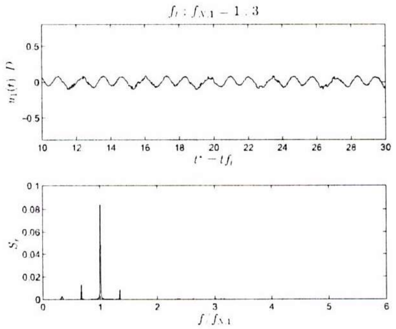

(a) $f_t : f_{N,1} = 1 : 3$.

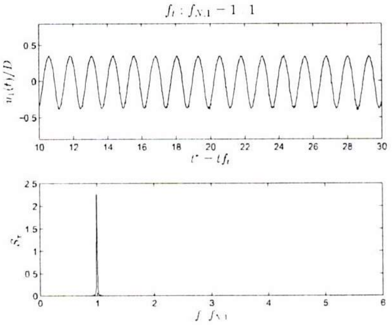

(b) $f_t : f_{N,1} = 1 : 1$.

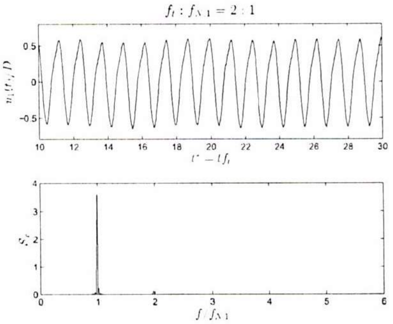

(c) $f_t : f_{N,1} = 2 : 1$.

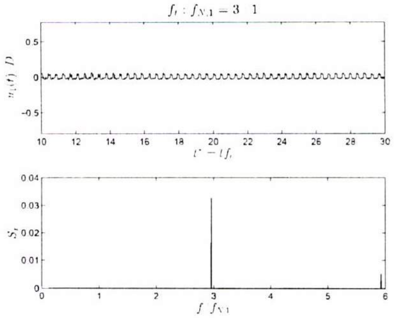

(d) $f_t : f_{N,1} = 3 : 1$.

FIGURE 8. Modal amplitude time series $u_1(t)/D$ and corresponding PSD.

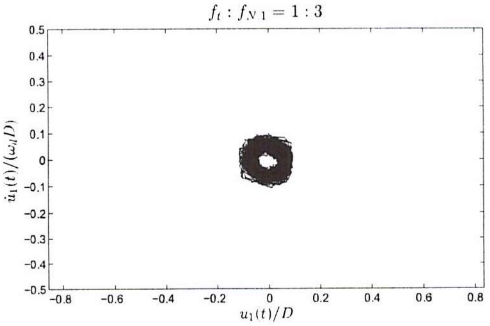

(a) $f_t : f_{N,1} = 1 : 3$.

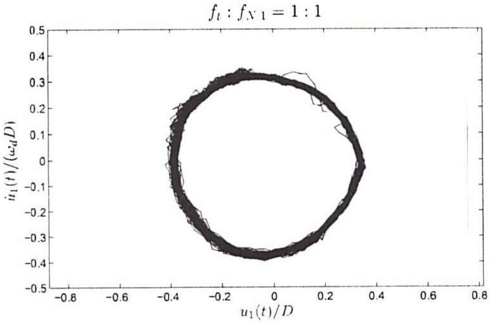

(b) $f_t : f_{N,1} = 1 : 1$.

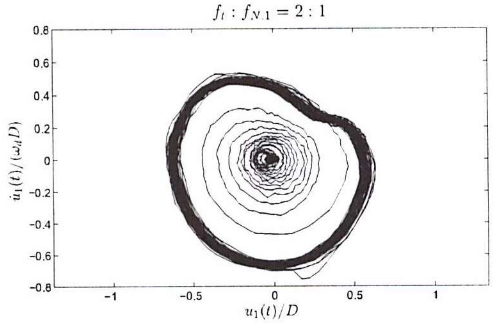

(c) $f_t : f_{N,1} = 2 : 1$.

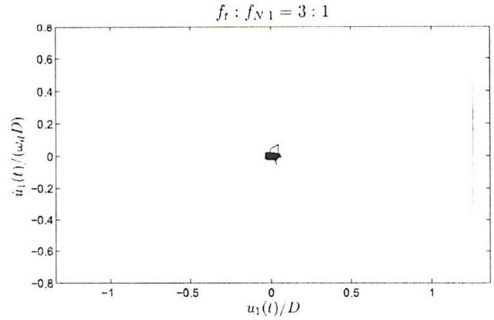

(d) $f_t : f_{N,1} = 3 : 1$.

FIGURE 9. First mode phase portraits $\dot{u}_1/(\omega_d D)$ vs $u_1(t)/D$.

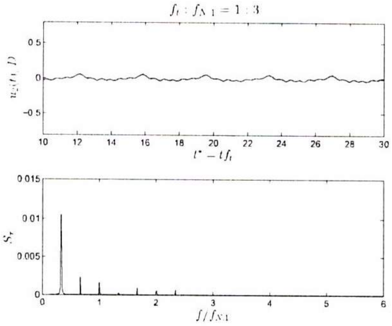

(a) $f_t : f_{N,1} = 1:3$.

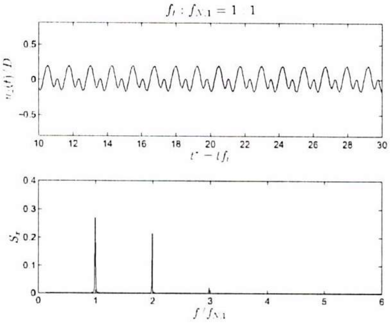

(b) $f_t : f_{N,1} = 1:1$.

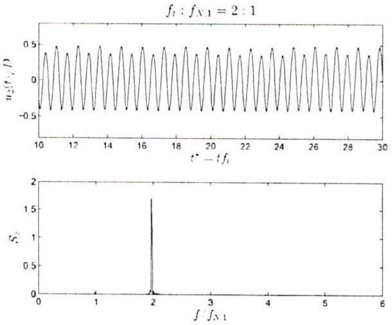

(c) $f_t : f_{N,1} = 2:1$.

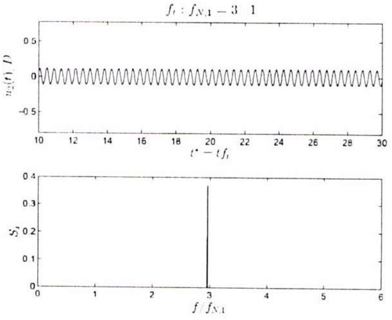

(d) $f_t : f_{N,1} = 3:1$.

FIGURE 10. Modal amplitude time series $u_2(t)/D$ and corresponding PSD.

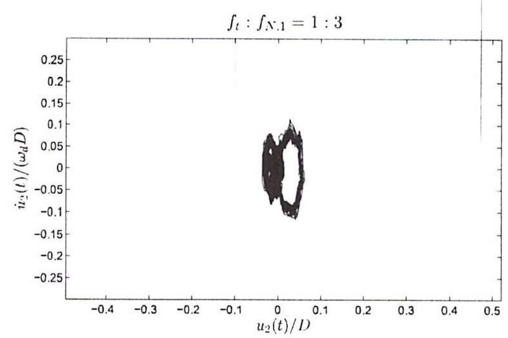

(a) $f_t : f_{N,1} = 1:3$.

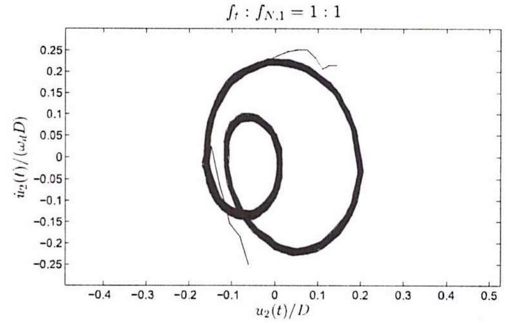

(b) $f_t : f_{N,1} = 1:1$.

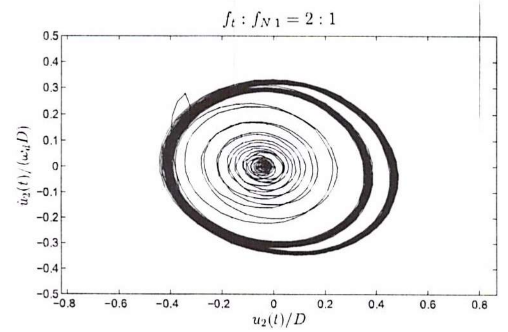

(c) $f_t : f_{N,1} = 2:1$.

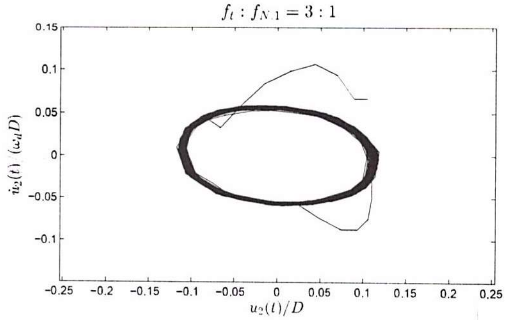

(d) $f_t : f_{N,1} = 3:1$.

FIGURE 11. Second mode phase portraits $\dot{u}_2/(\omega_d D)$ vs $u_2(t)/D$.

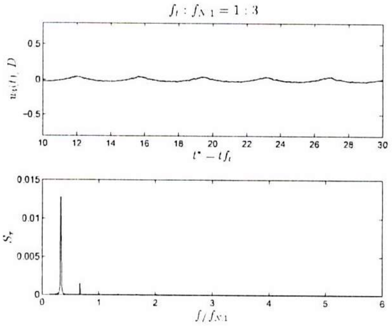

(a) $f_t : f_{N,1} = 1:3$.

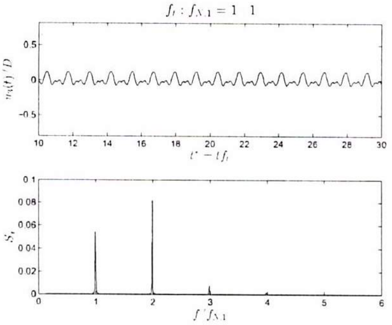

(b) $f_t : f_{N,1} = 1:1$.

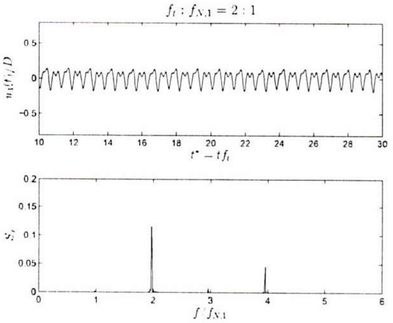

(c) $f_t : f_{N,1} = 2:1$.

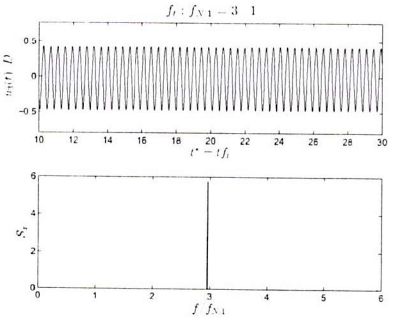

(d) $f_t : f_{N,1} = 3:1$.

FIGURE 12. Modal amplitude time series $u_3(t)/D$ and corresponding PSD.

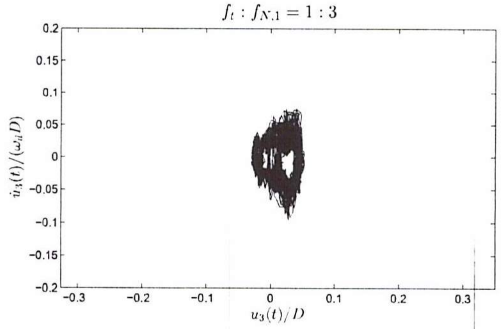

(a) $f_t : f_{N,1} = 1:3$.

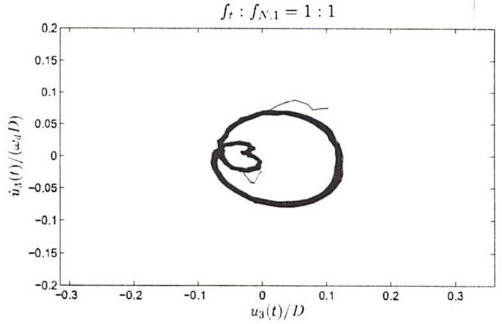

(b) $f_t : f_{N,1} = 1:1$.

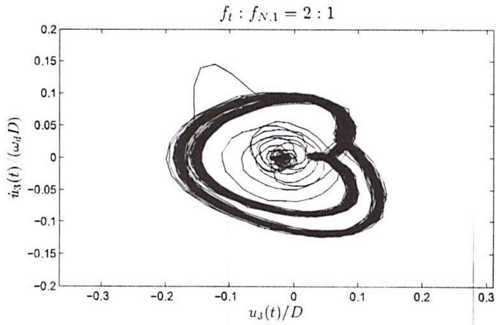

(c) $f_t : f_{N,1} = 2:1$.

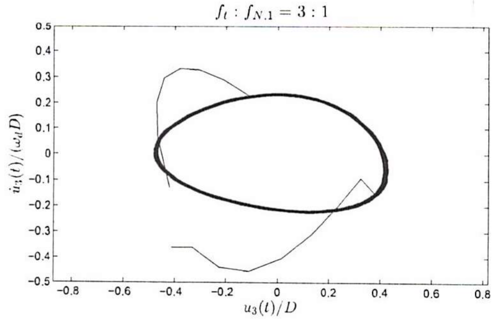

(d) $f_t : f_{N,1} = 3:1$.

FIGURE 13. Third mode phase portraits $\dot{u}_3/(\omega_d D)$ vs $u_3(t)/D$.